Performance changes of a grated waveguide at resonance wavelengths next to its band-edges due to modified edge sections

Husin Alatas,[1,2,*] Alexander A. Iskandar,[1] Hugo J. W. M. Hoekstra,[3] and May-On Tjia[1]

[1]*Physics of Magnetism and Photonics Research Group, Faculty of Mathematics and Natural Sciences, Institut Teknologi Bandung, Jl. Ganesha 10, Bandung 40132, Indonesia*
[2]*Theoretical Physics Division, Department of Physics, Bogor Agricultural University, Jl. Meranti, Kampus IPB Darmaga, Bogor 16680, Indonesia*
[3]*Integrated Optical MicroSystems Group, MESA+ Research Institute for Nanotechnology, University of Twente, P.O. Box 217, 7500 AE Enschede, The Netherlands*
**Corresponding author: alatas@ipb.ac.id*

Received May 17, 2010; revised September 20, 2010; accepted October 14, 2010; posted October 14, 2010 (Doc. ID 128535); published November 18, 2010

An efficient numerical scheme developed on the basis of Green's function method is applied to the investigation of structural effects on the performance of planar grated waveguide at the first resonance wavelengths next to the band-edges. Restricting ourselves to the transverse-electric waves, this study is focused on the effects induced by variations of the grating cell number and the depths of its four outer grooves on both sides. The different patterns of groove depth gradation or apodization considered in this study are all characterized by decreasing depth toward the ends while retaining the longitudinal grating symmetry. The effects of the modifications are expressed in terms of changes in the modal transmittance, reflectance, and out-of-plane scattering loss as well as the group velocity and resonant field enhancement. The most favorable result characterized by 15% transmittance enhancement and 85% loss reduction is achieved for the case with the most gradual changes in the groove depth. It is further shown that, for the investigated range of parameters, both the group velocity and field enhancement can best be improved by increasing the length of the uniform grating, without introducing any modification. © 2010 Optical Society of America

OCIS codes: 050.2770, 230.7400.

1. INTRODUCTION

The results of early studies on photonic crystals (PhCs) and their potential functionalities [1–3] have led to worldwide research activities for the development of a new generation of photonic devices. To that end, a large variety of three-dimensional (3D), two-dimensional (2D), and one-dimensional (1D) PhC structures have been considered, and their promising applications as building blocks of novel and high performance photonic devices have been demonstrated both numerically [4–9] and experimentally [4,10–15]. Unfortunately, the technology for precisely controlled fabrication of reproducible 3D device at the submicron- and nano-feature size has yet to be fully developed. On the other hand, the fabrication of quasi-2D planar PhC structure considered in the grated waveguide (GWg) systems is more amenable to the existing fabrication technology [16]. As a result, more reliable experimental verification of the numerical models can be performed on these systems as reported in [16–20]. This type of structures, while relatively simplified, still offer a large enough room for the exploration of a wide ranging applications with enhanced and new functionalities [19].

Studies of planar GWg systems and their promising applications have been reported previously by a number of research groups [17–22], and different numerical tools have been developed by different research groups such as the method of lines, finite difference time domain, eigenmode expansion, etc. [8,23]. Aside from the desirability for further exploration of the system functionalities, one has to address the ubiquitous problems concerning the out-of-plane scattering loss due to mode mismatch between the modal fields of the un-grated section and that of the grated section of the structure. Previous studies aiming at the reduction of loss and enhancement of planar GWg functionalities have been mostly restricted to the considerations of a variety of uniform grating structures of different geometries such as different duty cycles, mark-space ratios, and different index contrasts [22,23]. Possible effects of more detailed local structural variations in the graded structures have been for some reason largely left unexplored.

The graded grating structures have also been considered extensively for improving the performance of fiber Bragg grating (FBG) systems, leading to what is known as apodized FBG. The gradation of the grating structure was studied in detail for optimizing the spectral and dispersion characteristics of FBG in the design of optical wave filters used in wavelength division multiplexing (WDM) system [24]. The general and efficient differential inverse scattering formulations implemented with genetic algorithm [5] and layer-peeling algorithm [6,7] have been developed for the synthesis of FBG. The apodized grated

 © 2010 Optical Society of America

structure designed by those methods can be tailored to meet the required spectral characteristics for specific applications.

In the present study, a numerical scheme implemented on the basis of rigorous *ab initio* Green's function method following Dyson formulation [25–27] is employed to investigate the local structural effects of planar GWg. Compared to the other methods used for the study of planar GWg [8,23] and FBG systems [4–7], this formulation has the advantage of being quite efficient for handling perturbations due to local structural variations in a limited small area. Further, the computational window can be made relatively small owing to the built-in perfectly transparent boundary condition, which is typical for the Green's function method.

We consider in this work a number of GWg systems with uniformly grated central parts of various lengths and systematically modified edge sections of four grating teeth. The results reported here describe the effects of those structural variations on the device performance parameters such as its transmittance (T), reflectance (R), and loss (L), as well as the group velocity and the confined energy stored inside the GWg. The study will be focused on the device performance at the first resonance wavelengths next to the band-edges, since the operation at these wavelengths will help to meet the very much sought-after merits of high wavelength selectivity and sensitivity for high performance optical filters, resonators, and optical sensors.

The rest of this paper is organized as follows. In Section 2 the Green's function formalism and its numerical implemented scheme are discussed. In Section 3 the basic grating structure is introduced along with the structural modifications considered, as well as the performance parameters to be evaluated. The computational results and the related discussion are presents in Section 4. The paper ends with a summary given in Section 5.

2. GREEN'S FUNCTION AND ITS NUMERICAL FORMULATION

In the following explanation of the Green's function method, we suppress the time dependent factor of $\exp(-i\omega t)$ in the electric field expression. The basic three-layer structure of the system considered is shown in Fig. 1. For this system, the zz component of the transverse-electric (TE)-mode Green's tensor is obtained from the following implicit equation [25]:

$$G(\boldsymbol{r},\boldsymbol{r}') = G^B(\boldsymbol{r},\boldsymbol{r}') + \int_A G^B(\boldsymbol{r},\boldsymbol{r}'')k_0^2\Delta\varepsilon(\boldsymbol{r}'')G(\boldsymbol{r}'',\boldsymbol{r}')dA'', \tag{1}$$

where $(\boldsymbol{r},\boldsymbol{r}')=(x,y,x',y')$, $k_0=\omega/c$ is the free-space wave number, $\Delta\varepsilon=\varepsilon-\varepsilon_B$ is the contrast between the permittivities of the scatterer (ε) and background (ε_B), while A is the area of integration covering the entire computational domain. The background Green's function G^B in Eq. (1) for the corresponding three-layer background medium is determined as follows in terms of its Fourier components, m_l, pertaining to the lth layer [26]:

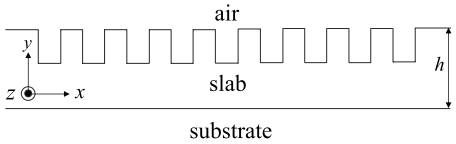

Fig. 1. Basic uniform GWg.

$$G_l^B(\boldsymbol{r},\boldsymbol{r}') = \frac{i}{4\pi}\int_{-\infty}^{\infty} dk_x \exp[ik_x(x-x')]m_l(k_x;y,y'), \tag{2}$$

where y and y' denote the observation point and the position of the unit source, respectively. The m_l function is expressed as a combination of the up-going (A_l) and down-going (B_l) wave amplitudes:

$$m_l = \frac{k_x^2}{k_{l,y}}[A_l(y,y')\exp(ik_{l,y}y) + B_l(y,y')\exp(-ik_{l,y}y)], \tag{3}$$

with $k_{l,y}=\sqrt{k_l^2-k_x^2}$ ($\mathrm{Re}(k_{l,y})\geq 0$) and $l=1,2,3$ as labels for the air, slab, and substrate layers, respectively. Further, each of those amplitudes is decomposed into its two components: $A_l=A_l^I+A_l^D$, $B_l=B_l^I+B_l^D$, with the superscripts I denoting the indirect contributions of the source via reflection or refraction and D denoting the direct contribution of the source in the l-layer. The integral in Eq. (2) is to be evaluated in the complex k_x-space. By following the procedure given in [26,27], we obtain the following expressions for the A_l and B_l amplitudes for layer l in the case where the source and the observation points are located in the same layer:

$$A_1^I = \exp(-ik_{1,y}h)\left[\frac{f_{1,2}+f_{2,3}\exp(2ik_{2,y}h)}{1+f_{1,2}f_{2,3}\exp(2ik_{2,y}h)}\right]\exp(ik_{1,y}y'),$$

$$A_1^D = \Theta(y-y')\exp(-ik_{1,y}y'), \tag{4}$$

$$B_1^I = 0,$$

$$B_1^D = \Theta(y'-y)\exp(ik_{1,y}y'), \tag{5}$$

$$A_2^I = \frac{f_{2,3}\exp(ik_{2,y}h)}{1-f_{2,1}f_{2,3}\exp(2ik_{2,z}h)}[f_{2,1}\exp(ik_{2,y}h)\exp(-ik_{2,y}y') + \exp(ik_{2,y}y')],$$

$$A_2^D = \Theta(y-y')\exp(-ik_{2,y}y'), \tag{6}$$

$$B_2^I = \frac{f_{2,1}\exp(ik_{2,y}h)}{1-f_{2,1}f_{2,3}\exp(2ik_{2,y}h)}[f_{2,3}\exp(ik_{2,y}h)\exp(ik_{2,y}y') + \exp(-ik_{2,y}y')],$$

$$B_2^D = \Theta(y'-y)\exp(ik_{2,y}y'), \tag{7}$$

$$A_3^I = 0,$$

$$A_3^D = \Theta(y-y')\exp(-ik_{3,y}y'), \tag{8}$$

$$B_3^I = \exp(-ik_{3,y}h)\left[\frac{f_{3,2}+f_{2,1}\exp(2ik_{2,y}h)}{1+f_{3,2}f_{2,1}\exp(2ik_{2,y}h)}\right]\exp(-ik_{3,y}y'),$$

$$B_3^D = \Theta(y' - y)\exp(ik_{3,y}y'), \tag{9}$$

where h denotes the slab thickness, while Θ represents the step function. Note that there are no indirect contributions to B_1 and A_3 due to the semi-infinite structure of the two outer layers.

For the case where the observation points are located in different layers, the corresponding amplitudes can be derived by using transfer matrix taking into account the continuity conditions. The result for $y > y'$ is given as follows:

$$\begin{pmatrix} A_l \\ B_l \end{pmatrix} = \gamma_{y>y'} \begin{pmatrix} \exp[id_l(k_{l+1,y} - k_{l,y})] & f_{l,l+1}\exp[-id_l(k_{l+1,y} + k_{l,y})] \\ f_{l,l+1}\exp[id_l(k_{l+1,y} + k_{l,y})] & \exp[-id_l(k_{l+1,y} - k_{l,y})] \end{pmatrix} \begin{pmatrix} A_{l+1} \\ B_{l+1} \end{pmatrix}, \tag{10}$$

and for $y < y'$,

$$\begin{pmatrix} A_l \\ B_l \end{pmatrix} = \gamma_{y<y'} \begin{pmatrix} \exp[id_{l-1}(k_{l-1,y} - k_{l,y})] & f_{l,l-1}\exp[-id_l(k_{l-1,y} + k_{l,y})] \\ f_{l,l-1}\exp[id_{l-1}(k_{l+1,y} + k_{l,y})] & \exp[-id_{l-1}(k_{l-1,y} - k_{l,y})] \end{pmatrix} \begin{pmatrix} A_{l-1} \\ B_{l-1} \end{pmatrix}, \tag{11}$$

where the coefficients γ's are defined as $\gamma_{y>y'} = (k_{l+1,y} + k_{l,y})/2k_{l+1,y}$, $\gamma_{y<y'} = (k_{l,y} + k_{l-1,y})/2k_{l-1,y}$, and the parameters d_1 and d_2 are chosen to be $d_1 = h$, $d_2 = 0$ as specified later in Fig. 2. The Fresnel coefficients $f_{l,l\pm1}$ in Eqs. (4)–(11) are given by

$$f_{l,l\pm1} = \frac{k_{l,y} - k_{l\pm1,y}}{k_{l,y} + k_{l\pm1,y}}. \tag{12}$$

Given the analytical expressions for the amplitudes with all the coefficients defined above, the integral in Eq. (2) can be computed numerically and efficiently by using the Gauss–Kronrod quadrature [27].

Having obtained the numerical result for $G^B(\boldsymbol{r},\boldsymbol{r}')$, the Green's function $G(\boldsymbol{r},\boldsymbol{r}')$ in Eq. (1) can be determined numerically by solving the discretized equation:

$$G_{ij} = G_{ij}^B + \sum_{\substack{i=1,j=1,\\ i\neq k, j\neq k}}^{P} G_{ik}^B k_0^2 \Delta\varepsilon_k \Delta A_k G_{kj} + M_i k_0^2 \Delta\varepsilon_i G_{ij} - L\frac{\Delta\varepsilon_i}{\varepsilon_B} G_{ij}, \tag{13}$$

where $G_{ij} \equiv G(r_i, r_j')$, the summation runs over all P mesh points, while the M_i and L parameters are introduced to handle the Green's function singularity according to the expressions given in [28]. However, instead of solving Eq. (1) directly, we adopt the simpler scheme introduced in [25] in which the contribution of each scatterer mesh is added one by one recursively.

With the result for the Green's function at hand, the electric field can be determined from the following explicit Dyson equation:

$$E_z(\boldsymbol{r}) = E_z^B(\boldsymbol{r}) + \int_A G(\boldsymbol{r},\boldsymbol{r}')k_0^2 \Delta\varepsilon(\boldsymbol{r}')E_z^B(\boldsymbol{r}')d\boldsymbol{r}', \tag{14}$$

where E_z^B is the electric field of the fundamental TE-mode of the effective slab waveguide, while A covers the entire computational window.

3. BASIC STRUCTURE, ITS MODIFICATIONS, AND CONSIDERED PERFORMANCE PARAMETERS

The GWg systems considered in this study are composed of different grating sections etched into a slab having a thickness of $h = 160$ nm as described in Fig. 2. The core section in the middle of the GWg is a uniformly grated part of N teeth with a 100 nm groove depth ($g = 100$ nm), for $N = 8$, 10, or 12. Each of the edge sections consists of four grooves with depths denoted by g_i's where $i = 1,2,3,4$. We choose the refractive indices of the materials as denoted in Fig. 2 and a fixed periodicity of $\Lambda = 200$ nm with 0.5 duty cycle for all grating sections, while the electromagnetic field is assumed to propagate in the x direction with TE polarization along the z direction (s-wave). In this work, the effects of changing the structural parameters (except Λ, the duty cycle, and g) on the operational characteristics will be systematically investigated for cases of different N's.

The considered structural variations cover 12 different combinations specified by the aggregate groove-depth parameters on the edge sections g_1, g_2, g_3, g_4 as arranged in Table 1. Note that the serial numbers have been chosen in

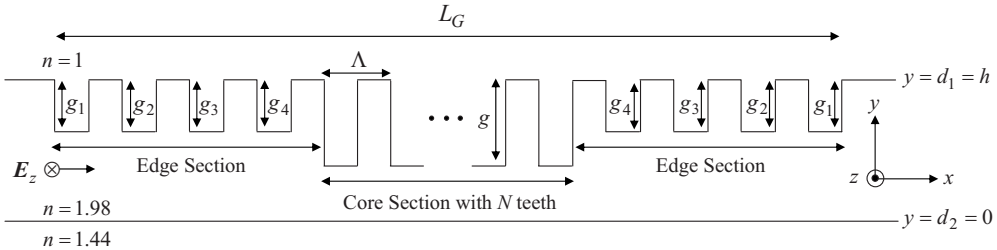

Fig. 2. GWg structures considered with the modifications at the edge described by the aggregate groove-depth parameters (g_1,g_2,g_3,g_4) and the number of teeth N in the core section.

Table 1. Modified Edge Grating Structures Corresponding to Aggregate Groove-Depth Parameters and the Associated Serial Numbers for the Resulting Structures

No.	g_1 (nm)	g_2 (nm)	g_3 (nm)	g_4 (nm)
1	0	0	0	0
2	20	20	20	20
3	40	40	40	40
4	20	40	60	80
5	40	40	60	80
6	40	60	60	80
7	60	60	60	60
8	60	60	60	80
9	60	60	80	80
10	60	80	80	80
11	80	80	80	80
12	100	100	100	100

the order of increasing total groove area of the edge sections. Further, the GWg's structures no. 1 and no. 12 actually correspond to the regular GWg with N and $N+8$ teeth, respectively.

Next, we introduce the evaluated parameters relevant for the device performance, which will be discussed in the following section. The modal transmittance (T) and reflectance (R) of the system are to be calculated at external positions x_i and x_t, located at distances of 10^3 and 3×10^3 nm from the left end and right ends of the device, respectively. The chosen positions are sufficiently far from the grating ends to ensure insignificant contributions from the scattered fields. These two quantities are calculated according to the following definitions:

$$T=\frac{\int_0^h |E_z(x_t,y;\lambda)|^2dy}{\int_0^h |E_{z,0}(x_i,y;\lambda)|^2dy}, \tag{15}$$

$$R=\frac{\int_0^h |E_z(x_i,y;\lambda)-E_{z,0}(x_i,y;\lambda)|^2dy}{\int_0^h |E_{z,0}(x_i,y;\lambda)|^2dy}, \tag{16}$$

where $E_z(x_t,y;\lambda)$ is the total external field at a position x_t and $E_z(x_i,y;\lambda)$ is the total field at a position x_i, while $E_{z,0}(x_i,y;\lambda)$ is the guided fundamental modal field at x_i. Using the calculated T and R for each case, one can determine the out-of-plane scattering loss L by applying the following relation:

$$L=1-T-R. \tag{17}$$

Next, the normalized group velocity (v_g/c) is determined on the basis of the following equation [29]:

$$\frac{v_g}{c}=-\frac{2\pi L_G}{\lambda^2 d\phi/d\lambda}. \tag{18}$$

In this expression L_G is the total length of the whole grated structure including the core and edges, while ϕ is the phase of the following complex transmission coefficient:

$$t=\frac{\int_0^h E_z(x_R,y;\lambda)dy}{\int_0^h E_{z,0}(x_L,y;\lambda)dy}, \tag{19}$$

where x_L and x_R denote the positions of the left and right grating ends, respectively. In addition to the above parameters, we also investigate the energy confinement effect by calculating the total energy confined, W, within a certain area A,

$$W=\int_A \varepsilon_{\text{slab}}|E|^2dA, \tag{20}$$

where A covers the non-GWg area in a fixed core section of eight teeth for all cases.

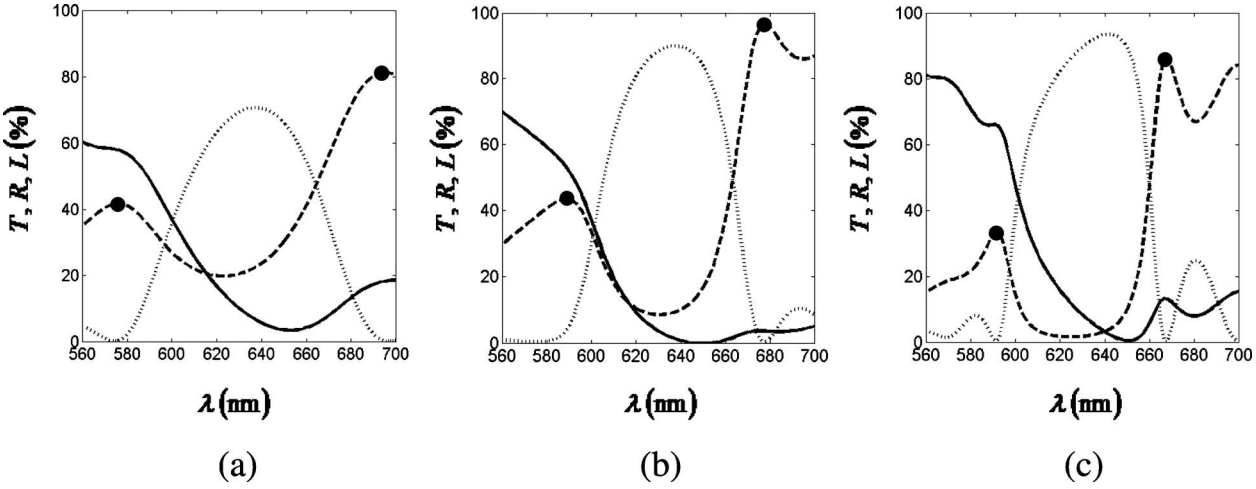

Fig. 3. Calculated spectral profiles of $T(\lambda)$ (dashed-line), $R(\lambda)$ (dotted-line), and $L(\lambda)$ (solid-line) presented for the GWg structures of (a) no. 1, (b) no. 6, and (c) no. 12 with $N=8$, as specified in the text. The solid dots indicate the position of resonance wavelength.

4. RESULTS AND DISCUSSION

The computational window chosen for the numerical study is defined along the x-axis by $[x_l,x_r]=[0,8]\times10^3$ nm and by $[y_l,y_u]=[-0.04,0.2]\times10^3$ nm along the y-axis. For the discretization, a rectangular mesh of area $\Delta A=2\times10^2$ nm^2 is chosen, with $\Delta x=10$ nm and $\Delta y=20$ nm, which has proved small enough to give convergent results.

The spectral profiles of $T(\lambda)$, $R(\lambda)$, and $L(\lambda)$ are calculated over the entire wavelength range of the bandgap and covering both of its edges for each of the GWg structures denoted by the numbers from 1 to 12. This calculation is separately carried out for cases with $N=8$, 10, and 12. In order to better exhibit the characteristic effects induced by structural changes of the GWg system, the calculated results are presented in Fig. 3 for only three distinct cases with GWg structures of nos. 1, 6, and 12 with $N=8$. It is observed that the resonance wavelengths corresponding to maximum transmittance at the left and right edges of the bandgap show opposite shifts as the structure varies from no. 1 to no. 12 (see Fig. 4). It is important to note that $L(\lambda)$ attains its remarkably smaller values for case no. 6 around the right resonance wavelength. On the other hand, $L(\lambda)$ appears to increase monotonously with respect to the same order of structural variation around the left resonance. It is obvious that its values at the left resonances are generally too large to be of practical interest.

The following discussion will be focused on the structure-modification-induced changes in the device operational parameters at resonances. Figure 5 shows the variations of $T(\lambda_{res})$ [Fig. 5(a)], $R(\lambda_{res})$ [Fig. 5(b)], and $L(\lambda_{res})$ [Fig. 5(c)] at both the left and right resonances (at the left and right panels, respectively) as the results of detailed structural changes over the entire range of the edge grating variation from no. 1 to no. 12. These calculations are performed separately for the cases with $N=8$, 10, and 12. We note that all three parameters (T,R,L) at each resonance wavelength display generally consistent patterns of variations for the three cases of different N's. However, it is also clear that the variation patterns at the left and right resonances are distinctly different. First, the reflectance (R) at the right resonance shows a pronounced "immunity" to the structural changes which clearly does not hold for the left resonance as shown by comparing the two panels in Fig. 5(b). Second, combining this $R(\lambda)$ with the $T(\lambda)$ spectral profiles depicted in Fig. 5(a), a remarkably low and relatively flat minimum loss at the right resonance is found as shown in Fig. 5(c), indicating a certain degree of robustness against structural changes. In particular, the loss reduction calculated for GWg structure no. 6 is about 85.3% for $N=10$, which is only slightly different from those for the structures with $N=8$ and 12. This result is consistent with the increasing adiabatic effect introduced by more gradually varied groove depth at the edge sections of the device. This effect is demonstrated by the calculated result presented in Fig. 6, where T, R, and L are plotted with respect to the variation of edge grating section in the order of decreasing the

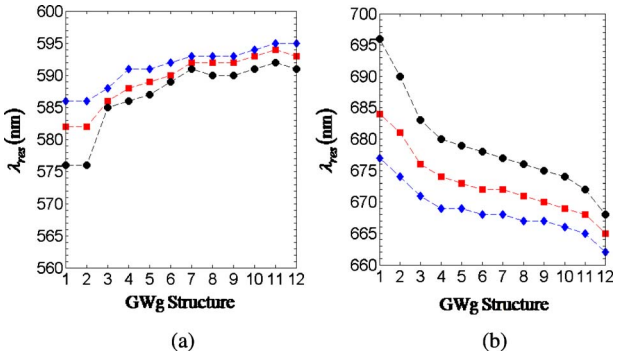

Fig. 4. (Color online) Variations of resonance wavelength showing the qualitatively different and generally opposite trends of shift with respect to structural variation from no. 1 to no. 12 for $N=8$ (black circles), 10 (red squares), and 13 (blue diamonds) at left (a) and (b) right.

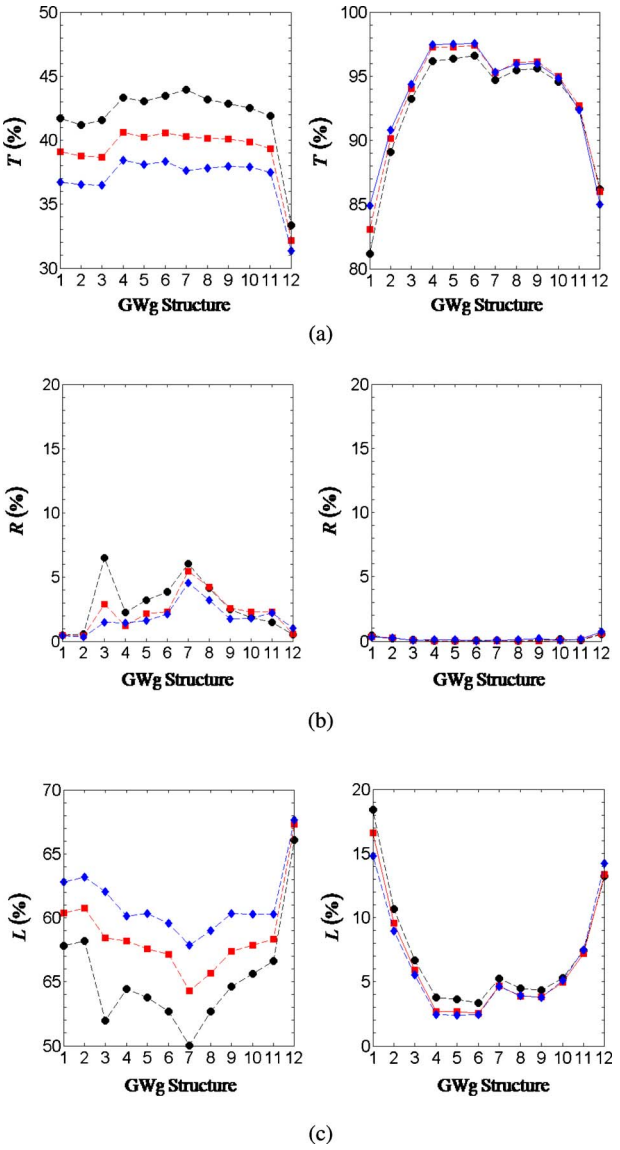

Fig. 5. (Color online) Variations of (a) T, (b) R, and (c) L at left resonances (left panels) and right resonances (right panels) for $N=8$ (black circles), 10 (red squares), and 12 (blue diamonds). Note the consistently flat responses to structural changes of R (b) on the right panel as compared to the relatively complicated albeit consistent responses shown on the corresponding left panel for different N's.

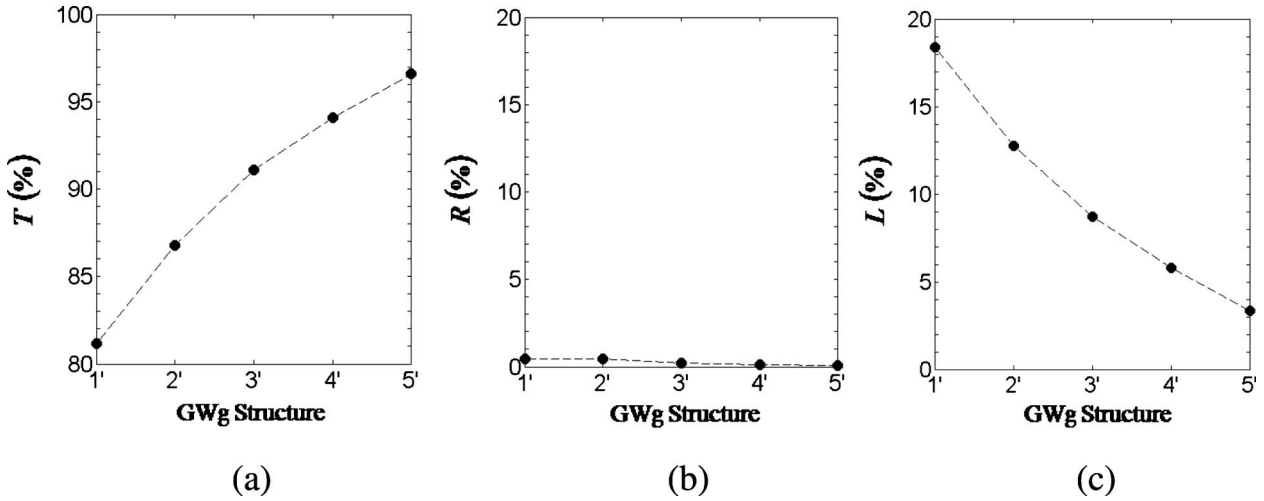

Fig. 6. Variations of (a) T, (b) R, and (c) L at left resonances (left panels) and at right resonances (right panels) with respect to modifications in the sequence marked by edge grating parameters: 1′. (0, 0, 0, 80) nm, 2′. (0, 0, 60, 80) nm, 3′. (0, 60, 60, 80) nm, and 4′. (40, 60, 60, 80) nm in increasing smoothness of the $\{g_i\}$ gradation.

abruptness between neighboring g_i's, namely, 1′. (0, 0, 0, 80) nm, 2′. (0, 0, 60, 80) nm, 3′. (0, 60, 60, 80) nm, and 4′. (40, 60, 60, 80) nm.

We turn next to the variations of group velocity and energy confinement effect. The calculated results are presented for the cases of left and right resonances in the left and right panels of Fig. 7, respectively. Interestingly, the normalized group velocity shown in Fig. 7(a) exhibits similar and generally decreasing v_g/c at both resonances for different N's. Meanwhile, the same structural changes also produce qualitatively similar rising trends of energy confinement, W, at both left and right resonances as shown in Fig. 7(b), although the confinement effect at the right resonance is more pronounced. It is worthwhile to note that the remarkable loss reduction attained by the structural modifications considered here does not produce concurrent favorable effects on group velocity and energy confinement. Further inspection of Fig. 7 shows, however, that a larger N generally gives rise to a more favorable effect on both counts. In fact, the lowest v_g/c of 0.2707 and strongest energy confinement effect characterized by an enhancement factor of 2.21 are simply achieved by the uniform grating with the largest number of grooves considered here, i.e., $N=12$, or a grating of 20 teeth with uniform groove depths.

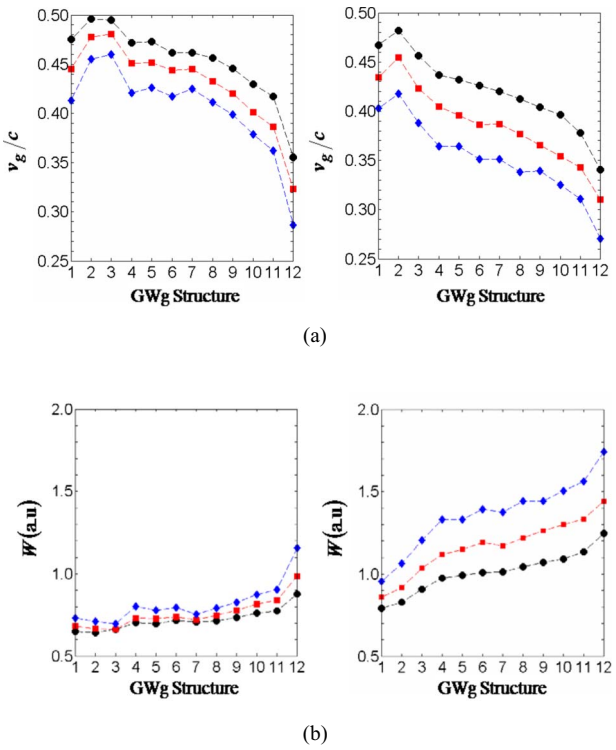

Fig. 7. (Color online) Comparisons between structure-variation-induced changes in at left resonances (left panels) and right resonances (right panels) of (a) the normalized group velocity and (b) the effect of energy confinement, W, for $N=8$ (black circles), 10 (red squares), and 12 (blue diamonds).

5. SUMMARY

We have studied, using the Green's function method, the changes in device performances at the first resonance wavelengths next to the band-edges of a grated waveguide (GWg) due to modification of the edge grating structures. The results of the numerical calculations show that the structure-modification-induced effects on the device operational characteristics differ distinctly at the left and right resonances. An appropriate modification of the edge grating having the smoothest graded structure has resulted in a most favorable transmittance enhancement of 14.9% and a maximum loss reduction of about 85.3% at the right resonance for the GWg structure no. 6 with $N=10$. It is also shown that enlarging the core grating section (increasing N) generally improves those two performance parameters. On the other hand, the normalized group velocity and energy confinement effect are not favorably affected by the changes of the GWg edge structure. Instead, simply increasing the length of uniform grating turns out to have significant favorable effects on both the group velocity and the energy enhancement effect.

ACKNOWLEDGMENTS

This work is supported by the Royal Netherlands Academy of Arts and Sciences (KNAW) through the Scientific Programme Indonesia-Netherlands (SPIN), project ref. no. 07-PD-12, and the Competence Research Grant from the Ministry of National Education of Indonesia (contract no. 223/SP2H/PP/DP2M/V/200). H. Alatas would like to thank L. O. Osapoetra for useful discussions.

REFERENCES

1. J. D. Joannopoulos, R. Meade, and J. Winn, *Photonic Crystals* (Princeton University Press, 1995).
2. J. D. Joannopoulos, P. R. Villeneuve, and S. Fan, "Photonic crystals: putting a new twist on light," Nature **386**, 143–149 (1997).
3. E. Yablonovitch, "How to be truly photonic," Science **289**, 557–559 (2000).
4. J. Skaar, B. Sahlgren, P.-Y. Fonjallaz, H. Storøy, and R. Stubbe, "High-reflectivity fiber-optic bandpass filter designed by use of the iterative solution to the Gel'Fand–Levitan–Marchenko equations," Opt. Lett. **23**, 933–935 (1998).
5. J. Skaar and K. M. Risvik, "A genetic algorithm for the inverse problem in synthesis of fiber gratings," J. Lightwave Technol. **16**, 1928–1932 (1998).
6. R. Feced, M. N. Zervas, and M. A. Muriel, "An efficient inverse scattering algorithm for the design of nonuniform fibre Bragg gratings," IEEE J. Quantum Electron. **35**, 1105–1115 (1999).
7. J. Skaar, L. Wang, and T. Erdogan, "On the synthesis of fiber Bragg grating by layer peeling," IEEE J. Quantum Electron. **37**, 165–173 (2001).
8. A. Lavrinenko, P. Borel, L. Frandsen, M. Thorhauge, A. Harpøth, M. Kristensen, T. Niemi, and H. Chong, "Comprehensive FDTD modelling of photonic crystal waveguide components," Opt. Express **12**, 234–248 (2004).
9. T.-T. Kim, S.-G. Lee, H. Y. Park, J.-E. Kim, and C.-S. Kee, "Asymmetric Mach–Zehnder filter based on self-collimation phenomenon in two-dimensional photonic crystals," Opt. Express **18**, 5384–5389 (2010).
10. S. Noda, "Recent progresses and future prospects of two- and three-dimensional photonic crystals," J. Lightwave Technol. **24**, 4554–4567 (2006).
11. M. Notomi, A. Shinya, S. Mitsugi, E. Kuramochi, and H. Y. Ryu, "Waveguides, resonators and their coupled elements in photonic crystal slabs," Opt. Express **12**, 1551–1561 (2004).
12. M. R. Lee and P. M. Fauchet, "Two-dimensional silicon photonic crystal based biosensing platform for protein detection," Opt. Express **15**, 4530–4535 (2007).
13. L. Lagonigro, N. Healy, J. R. Sparks, N. F. Baril, P. J. A. Sazio, J. V. Badding, and A. C. Peacock, "Low loss silicon fibers for photonics applications," Appl. Phys. Lett. **96**, 041105 (2010).
14. R. Colombelli, K. Srinivasan, M. Troccoli, O. Painter, C. F. Gmachl, D. M. Tennant, A. M. Sergent, D. L. Sivco, A. Y. Cho, and F. Capasso, "Quantum cascade surface-emitting photonic crystal laser," Science **302**, 1374–1377 (2003).
15. M. Imada, L. H. Lee, M. Okano, S. Kawashima, and S. Noda, "Development of three-dimensional photonic-crystal waveguides at optical-communication wavelengths," Appl. Phys. Lett. **88**, 171107 (2006).
16. H. Benisty, C. Weisbuch, D. Labilloy, M. Rattier, C. J. M. Smith, T. F. Krauss, R. M. De La Rue, R. Houdr'e, U. Oesterle, C. Jouanin, and D. Cassagne, "Optical and confinement properties of two-dimensional photonic crystals," J. Lightwave Technol. **17**, 2063–2077 (1999).
17. T. C. Kleckner, D. Modotto, A. Locatelli, J. P. Mondia, S. Linden, R. Morandotti, C. De Angelis, C. R. Stanley, H. M. Van Driel, and J. S. Aitchison, "Design, fabrication, and characterization of deep-etched waveguide gratings," J. Lightwave Technol. **23**, 3832–3842 (2005).
18. W. C. L. Hopman, R. Dekker, D. Yudistira, W. F. A. Engbers, H. J. W. M. Hoekstra, and R. M. de Ridder, "Fabrication and characterization of high-quality uniform and apodized Si_3N_4 waveguide gratings using laser interference lithography," IEEE Photon. Technol. Lett. **18**, 1855–1857 (2006).
19. W. C. L. Hopman, P. Pottier, D. Yudistira, J. Van Lith, P. V. Lambeck, R. M. De La Rue, A. Driessen, H. J. W. M. Hoekstra, and R. M. de Ridder, "Quasi-one-dimensional photonic crystal as a compact building block for refractometric optical sensors," IEEE J. Sel. Top. Quantum Electron. **11**, 11–16 (2005).
20. N. Destouches, B. Sider, A. V. Tishchenko, and O. Parriaux, "Optimization of a waveguide grating for normal TM mode coupling," Opt. Quantum Electron. **38**, 123–131 (2006).
21. H. J. W. M. Hoekstra, W. C. L. Hopman, J. Kautz, R. Dekker, and R. M. De Ridder, "A simple coupled mode model for near band-edge phenomena in grated waveguides," Opt. Quantum Electron. **38**, 799–813 (2007).
22. J.-W. Mu, H. Zhang, and W.-P. Huang, "Design of waveguide Bragg gratings with strong index corrugations," J. Lightwave Technol. **26**, 1596–1601 (2008).
23. J. Čtyroký, S. Helfert, R. Pregla, P. Bientsman, R. Baets, R. M. De Ridder, R. Stoffer, G. Klaasse, J. Petracek, P. Lalanne, J.-P. Hugonin, and R. M. De La Rue, "Bragg waveguide grating as 1D photonic band gap structure: COST 268 modelling task," Opt. Quantum Electron. **34**, 455–470 (2002).
24. R. Kashyap, *Fiber Bragg Gratings* (Academic, 1999).
25. J. M. Elson and K. Halterman, "Local density of states analysis of surface wave modes on truncated photonic crystal surfaces with nonlinear material," Opt. Express **12**, 4855–4863 (2004).
26. M. Paulus and O. J. F. Martin, "Green's tensor technique for scattering in two dimensional stratified media," Phys. Rev. E **63**, 066615 (2001).
27. M. Paulus, P. Gay-Balmaz, and O. J. F. Martin, "Accurate and efficient computation of Green's tensor for stratified media," Phys. Rev. E **62**, 5797–5807 (2000).
28. O. J. F. Martin and N. B. Piller, "Electromagnetic scattering in polarizable backgrounds," Phys. Rev. E **58**, 3909–3915 (1998).
29. J. M. Bendickson, J. P. Dowling, and M. Scalora, "Analytic expressions for the electromagnetic mode density in finite, one-dimensional, photonic band-gap structures," Phys. Rev. E **53**, 4107–4121 (1996).